Extended x-ray emission times of clusters in intense x-ray pulses

Phay J. Ho, Christopher Knight, and Linda Young

Phys. Rev. A **101**, 043413 — Published 23 April 2020

DOI: 10.1103/PhysRevA.101.043413

Extended X-ray Emission Times of Clusters In Intense X-ray Pulses

Phay J. Ho,[1,*] Christopher Knight,[2] and Linda Young[1,3]

[1] *Chemical Sciences and Engineering Division, Argonne National Laboratory, Argonne, Illinois 60439, USA*

[2] *Computational Science Division, Argonne National Laboratory, Argonne, Illinois 60439, USA*

[3] *Department of Physics and James Franck Institute, The University of Chicago, Chicago, Illinois 60637, USA*

Abstract

Recently, intensity correlation of x-ray fluorescence, based on the principle introduced by Hanbury Brown and Twiss, has been proposed for high-resolution imaging of a 3D arrangement of atoms. To explore the applicability of this fluorescence approach, we theoretically investigate fluorescence dynamics of non-periodic systems subject to XFEL pulses over a range of fluences from the linear to non-linear x-ray absorption regimes as a function of system size, from single atom to a cluster of 150k atoms. Fluorescence dynamics in the non-linear x-ray regime differs from that in the weak x-ray field in that intense x-ray pulses interrupt the fluorescence dynamics by multi-photon absorption creating a dense electron environment within the sample on a femtosecond timescale. In large systems, the presence of both recombination and photoionization pathways gives rise to an enhanced $K\alpha$ and $K\alpha^h$ emission yield and extended emission time beyond the lifetime of the core-excited states. Our analysis suggests that in an intense x-ray pulse, the $K\alpha^h$ emission line can be a good candidate for fluorescence imaging as it has a higher yield and an emission time short relative to the x-ray induced lattice distortion time.

* pho@anl.gov

I. INTRODUCTION

The advent of x-ray free-electron lasers has led to the development and exploration of novel high-resolution imaging approaches [1, 2]. Single-particle imaging based on the diffract-before-destroy approach using coherent x-ray diffraction (CXD) [3, 4] has enabled measurement of the structure of biological specimens [5, 6] and complex materials [7]. In addition, using pump-probe CXD, it has been possible to follow ultrafast light-induced structural and electron dynamics [8–10]. Despite continuous progress, it has remained a challenge [11] to achieve nm or sub-nm resolution and elemental contrast [12] due to the need to capture and classify a large number of scattering images with limited radiation damage during the pulse and to produce the scattering signals with high signal-to-noise ratio and high spatial resolution information [11, 13–16].

In conventional CXD, the fringes in the diffraction patterns result from the interference between the amplitudes of scattered light originating from atoms located within a sample. Because a fixed phase relationship between the incoming and scattered photon exists, the interference pattern reveals information about the spatial distribution of atoms. However, interference effects are not limited to the amplitude of the radiation field and higher order interferences can be used to extract structural information. Hanbury Brown and Twiss (HBT) demonstrated an interference effect between two light intensities [17]. Using the intensity correlation between two different points on the star Sirius, a random/thermal light source, they determined its angular size. The discovery of the HBT effect has inspired the formulation of the quantum theory of optical coherence [18] and the development of new imaging techniques that exploit intensity correlation for achieving enhanced resolution below the Abbe limit (classical diffraction limit) in visible range[19–25]. This approach has been further extended to vacuum ultraviolet for resolving the structure of 2-D objects [26].

Recently, Classen and coworkers [27] proposed to use single-shot intensity correlations to image the 3D arrangement of an array of heavy atoms using intense x-ray pulses – a technique they named "incoherent diffractive imaging". The general idea is that an ultrashort, intense x-ray pulse can excite the K-shell of a collection of heavy atoms, where the fluorescence quantum yield is high, and that the fluorescence angular distribution, recorded within their coherence time τ_c, where τ_c is related to the radiative lifetime (for Fe atoms, $\tau_c = h/\Gamma = 2.6$ fs), reflects the 3D atomic arrangement. By treating the heavy atoms as

random light emitters, the second order correlation function $G_2(\vec{k}_1, \vec{k}_2)$ of the fluorescence intensity measured at two momentum transfer vectors, $I(\vec{k}_1)$ and $I(\vec{k}_2)$, are related to the Fourier transform of the distribution of the fluorescence emitters $\rho_f(\vec{r})$ by the following relation

$$G_2(\vec{k}_1, \vec{k}_2) - 1 = \left| \int d^3 r \rho_f(\vec{r}) e^{i(\vec{k}_1 - \vec{k}_2)\cdot\vec{r}} \right| \tag{1}$$

where

$$G_2(\vec{k}_1, \vec{k}_2) = \frac{\langle I(\vec{k}_1) I(\vec{k}_2) \rangle}{\langle I(\vec{k}_1) \rangle \langle I(\vec{k}_2) \rangle}, \tag{2}$$

In comparison to the conventional CXD approach, the fluorescence intensity correlation method has the advantage that the probability of the fluorescence process is higher than the coherent scattering process in the x-ray regime, apart from Bragg scattering [27]. In addition, since the obtained fluorescence spectrum is sensitive to the x-ray photon energy and is element-specific, this approach can potentially be a powerful single-particle imaging technique that complements the coherent diffraction method and provides high-degree of elemental contrast heterogeneous materials and biological samples.

The EuXFEL and the upcoming LCLS-II, which can deliver intense few-fs pulses at high-repetition rates, will further facilitate this photon-hungry fluorescence intensity correlation measurement [26]. To fully exploit this approach, we need to understand the fluorescence process in a complex environment under irradiation of an intense x-ray XFEL to deduce optimal pulse conditions for this approach. In this context, the fluorescence emission time is an important consideration and is closely connected to the visibility of the intensity correlation function. When the emission time is longer than the coherence time, i.e. the lifetime of the fluorescence state [28], the obtained intensity correlation will have reduced visibility. This reduced visibility can be overcome by averaging over more many measurements to enhance the signal-to-noise ratio [17, 27]. Apart from the coherence time consideration, x-ray induced atomic motion during the fluorescence collection can also affect the effectiveness of this approach. Samples exposed to intense x-ray pulses will undergo ultrafast charging [29–33], starting from sequential photon absorption [34–40] within the XFEL pulse duration, followed by the overall sample electronic response and structural distortion [9, 10]. From our previous study of CXD of an inorganic cluster exposed to an intense XFEL pulse, an atomic motion of 1 Bohr radius or more during the x-ray pulse can reduce the visibility/contrast of the scattering pattern, i.e. the first -order correlation function [16]. We note that in the

XUV spectral regime fluorescence spectra have been observed using FEL pulses and used to identify transient states in rare-gas and core-shell clusters [41] and to study cluster excitation dynamics [42, 43]. But, the fluorescence pathways and emission times in extended systems interacting with intense x-ray pulses have not been studied to our knowledge.

In this paper, using Ar clusters as a prototypical system, we examined the fluorescence dynamics in XFEL pulse as a function of fluence and particle size. We found that the x-ray emission time in extended systems is dictated by not only by the x-ray pulse duration and lifetime of the core-excited states. [In this system, following [27], $\tau_c = h/\Gamma = 5.2$ fs for $\Gamma = 0.8$ eV [44].] Rather, ultrafast electron dynamics can greatly modify fluorescence characteristics by opening additional fluorescence pathways via electron-ion recombination in addition to the direct photoionization pathways. The existence of these two pathways gives rise to higher $K\alpha$ and $K\alpha^h$ yields in clusters. We show that the $K\alpha^h$ emission from an atomic site with a hollow K-shell can be a good candidate for fluorescence imaging as it has an emission time that is shorter than the x-ray induced lattice-distortion timescale.

II. METHOD

We use our Monte-Carlo/Molecular-Dynamics method to study the fluorescence processes in Ar clusters induced by intense x-ray free-electron pulses. In this method, the full electron and nuclear dynamics are modeled in an atomistic manner. The details of our method have been presented in the previous work [16, 45]. In brief, the interaction of the cluster with the incident XFEL pulse is treated quantum mechanically with a Monte Carlo method by tracking explicitly the time-dependent quantum transition probability between different electronic configurations. The total transition rate, Γ, between different electronic configurations I and J is given by

$$\Gamma_{I,J} = \Gamma^P_{I,J} + \Gamma^A_{I,J} + \Gamma^F_{I,J} + \Gamma^{RE}_{I,J} + \Gamma^{EI}_{I,J} + \Gamma^{RC}_{I,J}. \tag{3}$$

Starting from the ground state of the neutral atom, we include the contribution from photoionization $\Gamma^P_{I,J}$, Auger decay $\Gamma^A_{I,J}$, fluorescence $\Gamma^F_{I,J}$, resonant excitation $\Gamma^{RE}_{I,J}$, electron-impact ionization $\Gamma^{EI}_{I,J}$ and electron-ion recombination $\Gamma^{RC}_{I,J}$. Additionally, a molecular dynamics (MD) algorithm is used to propagate all particle trajectories (atoms/ions/electrons) forward in time (see Appendix for our scheme of activating and deactivating an electron in

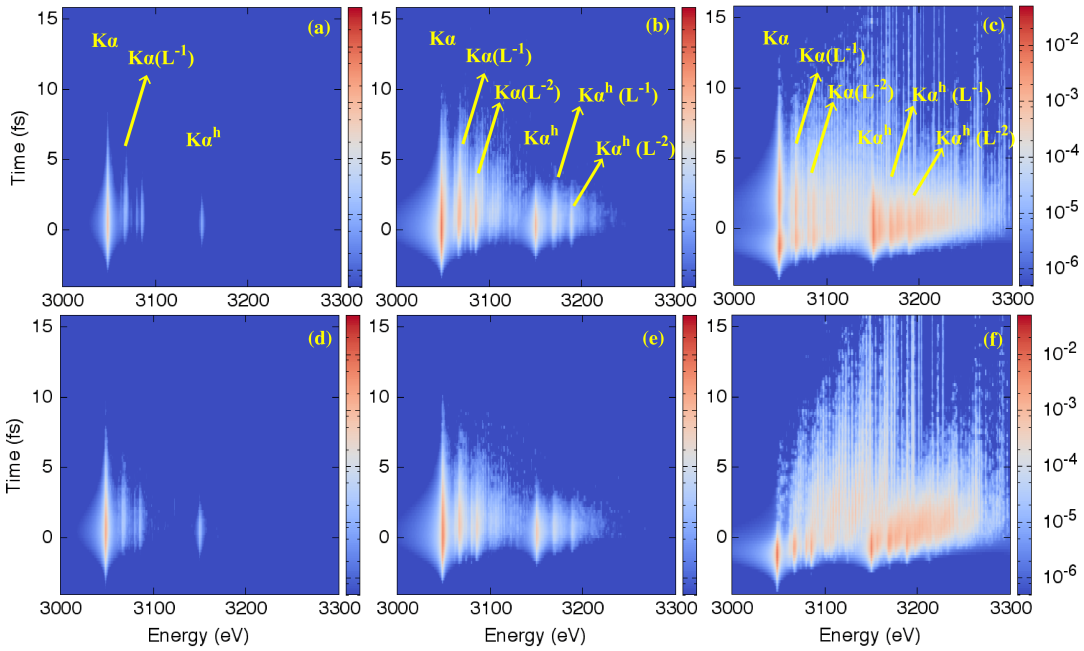

FIG. 1. (Color online) X-ray emission rate per atom in Ar_{1415} exposed to a 5-keV, 2-fs XFEL pulse with fluence of (a) 0.1 F_s (b) 1 F_s and (c) 10 F_s. The bottom row shows the result obtained for a single atom exposed to the same XFEL pulse with a fluence of (d) 0.1 F_s (e) 1 F_s and (f) 10 F_s.

our calculation).

By tracking the time evolution of electronic configurations of atoms and ions and their interaction with electrons, we investigated the effect of an intense x-ray field on the fluorescence dynamics of individual emission lines as a function of time, as well as the impact of particle size on the fluorescence yield and emission time. We note that the calculated transition rates of $K\alpha$ and $K\alpha^h$ based on Hartree-Fock-Slater model agree with the rates from Dirac-Hartree-Slater method that includes relativistic effects[46, 47].

The presence of the neighboring atoms, ions and electrons can gives rise to a lower ionization potential, so-called continuum lowering, and a shift in fluorescence lines. The model to accurately account for this is still currently being debated and is an intense research topic [48–51]. In this study, we focus on the general trend of the fluorescence process and the energy levels are unshifted.

For all calculations, the XFEL pulse is assumed to have a Gaussian temporal profile with

a photon energy of 5 keV and a FHWM pulse length of 2 fs. The 5-keV photon energy was selected because the results of MC/MD of Ar cluster [45] have shown to agree with the SACLA experimental Ar cluster data obtained at 5 keV[52]. The 2-fs pulse duration was motivated by our previous studies, which showed that the structure of Ar_{1415} remains intact during a 2-fs XFEL pulse with an intensity approaching 10^{21} W/cm^2, even though it can undergo substantial changes to its electronic structure [16]. In this study, we focus on fluence values in the range of 0.1 to 10 times the saturation fluence, F_s, for single ionization. More specifically, $F_s \approx 3.5 \times 10^{11}$ photons/μm^2 at 5 keV. These fluences correspond to 0.03 to 3 mJ pulses or $1.5{\times}10^{17}$ to $1.5{\times}10^{19}$ W/cm^2. These short pulses are currently accessible and will also be available in the upgraded facilities [53, 54]. Also, by examining Ar clusters of different sizes, our study illuminates the impact of a complex environment on fluorescence dynamics beyond that of an isolated atom.

To track the fluorescence events, a small time step of 2 attoseconds was used in the MC/MD calculations. Each calculation is computationally intensive as the probability of fluorescence is lower than Auger decay, especially in pulses with low fluence and in a small system. Thus, a large number of replicas is needed to obtain a converged temporal emission profile for each fluorescence line and its yield. For this study, the error in per atom yield of $K\alpha$ and $K\alpha^h$ emission is less than 0.1 %. We point out the fluorescence spectrum obtained from an ensemble of calculations with a time step of 2 as is statistically identical to the result computed with a time step of 0.2 as. Most of the calculations were completed on a local workstation. But, the calculations of two of our clusters, which require tracking of more than 10^6 particles (ions + electrons) were performed using Mira at the Argonne Leadership Computing Facility (ALCF).

III. RESULT

A. Fluence Dependence

In this paper, we focus on 2p $\rightarrow$ 1s fluorescence transitions from various charge states and electronic configurations since these transitions are typically localized on individual atom/ions. By studying their fluorescence yield and time emission profile, we can deduce optimal fluorescence channels and pulse strength for imaging in extended systems and com-

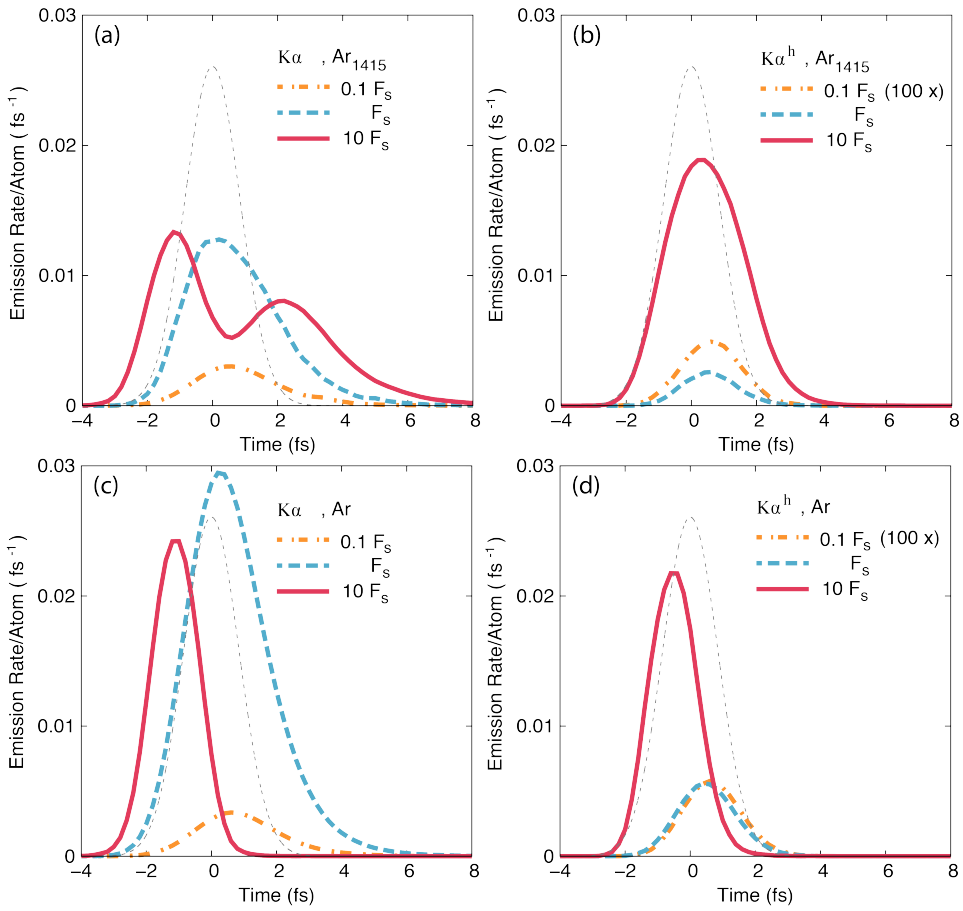

FIG. 2. (Color online) Fluence dependence of the temporal profile of (a) $K\alpha$ emission in Ar_{1415}, (b) $K\alpha^h$ emission in Ar_{1415}, (c) $K\alpha$ emission in Ar atom and (d) $K\alpha^h$ emission in Ar atom. The temporal profile of the $K\alpha^h$ emission of the cluster and atom at 0.1 F_s is amplified by a factor of 100. The dashed line in each plot shows the temporal x-ray profile.

plex molecules.

Figures 1 (a)-(c) plot the x-ray emission rate/atom from an Ar cluster as a function of time for fluorescence events for fluence values of 0.1, 1 and 10 F_s. These plots were obtained by binning the average number of fluorescence events/atom of each channel from an ensemble of MC/MD calculations in 0.1 fs time step. Fig. 1 (a) shows that at 0.1 F_s, the dominant fluorescence channel is $K\alpha$, which corresponds to the transition of a 2p electron filling the 1s core hole in a singly charged ion. The fluorescence yields from other satellites are negligible. At F_s, the contribution of fluorescence channels from doubly charged states increases. These channels include hypersatellite $K\alpha^h$ and satellite ($K\alpha(L^{-1})$), which correspond to relaxation

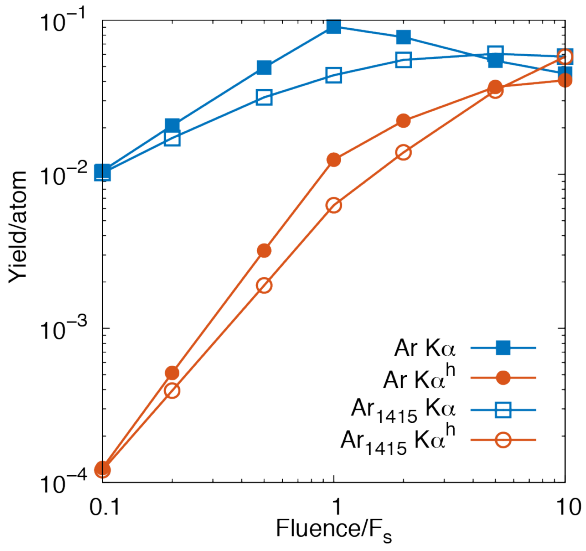

FIG. 3. (Color online) Fluence dependence of $K\alpha$ and $K\alpha^h$ yield/atom of Ar atom and Ar_{1415} in a 5-keV, 2-fs XFEL pulse.

from double core-hole state and doubly charge ions with a single vacancy in both K- and L-shell. At 10 F_s, fluorescence from higher charge states becomes probable, giving rises additional lines, such as $(K\alpha(L^{-2}))$ and $(K\alpha^h(L^{-1}))$, as shown in Fig. 1 (c).

Apart from the number of fluorescence channels, the temporal emission profile of individual lines is shown to depend on the fluence. Here, we focus on $K\alpha$ and $K\alpha^h$ emission profiles as they are the most dominant channels in our fluence range. Fig. 2 depicts that both the time window of $K\alpha$ and $K\alpha^h$ emission at 10 F_s are longer than those at lower fluences. This fluence dependence is not exhibited in isolated Ar atom. Fig. 2 shows that the temporal emission profile and the dominant fluorescence channels of an atom at 0.1 and 1 F_s are very similar to those found in the cluster. However, at 10 F_s, the time emission windows of $K\alpha$ and $K\alpha^h$ are shorter than those at lower fluences. Also, the comparison of Fig. 1 (c) and (f) shows that the fluorescence events from higher charge states are suppressed or restricted to a narrow time window in the cluster.

The difference is a result that the XFEL-induced electronic excitation and relaxation in a cluster are different than those in an isolated atom, leading to additional fluorescence pathways in a cluster. Before we describe these pathways, we will discuss the x-ray interaction with an atom and extended system in different fluences. Fig. 3 shows the fluorescence yield of $K\alpha$ and $K\alpha^h$ as a function of fluence for both the atom and cluster. In the weak-field

regime (0.1 to 1 F_s), the production of $K\alpha$ and $K\alpha^h$ of the isolated atom can be described by perturbation theory. Here, the $K\alpha$ yield increases linearly with fluence and the slope is 1, whereas the $K\alpha^h$ yield shows a quadratic dependence on the pulse fluence. Above F_s, the physics is dominated by a sequential multiphoton process, in which the rate of double core-hole state (DCHS) production can compete with the inner-shell decay rate. An increase in fluence leads to depletion of the single-core hole state (SCHS) population and, consequently, a reduction in $K\alpha$ yield and narrower x-ray emission time window, as shown in Fig. 2 (c). Also, the production of $K\alpha^h$ is correlated with the reduction of $K\alpha$ yield as the DCHS is produced by removing SCHS. In this nonperturbative regime, $K\alpha^h$ still increases with fluence, but it deviates from the quadratic dependence and has narrower x-ray emission time window than that in the perturbative regime.

In a cluster, the complexity of the dynamics is compounded by the interaction between atoms and between delocalized electrons. Both electron impact ionization and electron-ion recombination play an important role in the fluorescence dynamics. Below F_s, the cluster $K\alpha$ and $K\alpha^h$ yield are smaller than the atom, and $K\alpha$ and $K\alpha^h$ deviate from linear and quadratic dependence respectively. This is because electron-impact ionization, which is absent in isolated atom, depletes single- and double-core-hole states. In the nonperturbative regime, both the $K\alpha$ and $K\alpha^h$ yield of the cluster are found to overtake those of atom above 5 F_s, indicating that the presence of additional pathways in the cluster. These pathways involve electron-ion recombination and their high probability is enabled by a dense electron environment created in the cluster. In the case of $K\alpha$, its fluorescence state can be generated from an electron recombining with Ar^{2+} ions with electron configuration of $1s2s2p^63s^23p^6$, $1s2s^22p^53s^23p^6$ and others by filling the vacancy in the L or M shell. Fig. 4 shows one example of the recombination pathways. We point out that the previous work by Iwayama and coworkers have observed fluorescence from the electronic transition 4d $\rightarrow$ 3p due to delocalized electrons recombining with multiply charged Ar ions in cluster [42].

Fig. 4 (b) shows that, at 10 F_s, the $K\alpha$ emission via the photoionization pathways peaks at t = -1 fs, whereas the emission via the recombination pathways peaks at t = 2.2 fs. In particular, Fig. 4 (d) shows that the atoms that undergo $K\alpha$ via the recombination pathways have a maximum average charge state of 4.3, which means that these atoms undergo about 3 or more recombination events to reach the fluorescence state (SCHS). If the fluence is increased to 100 F_s, the most probable fluorescence events via recombination pathway are

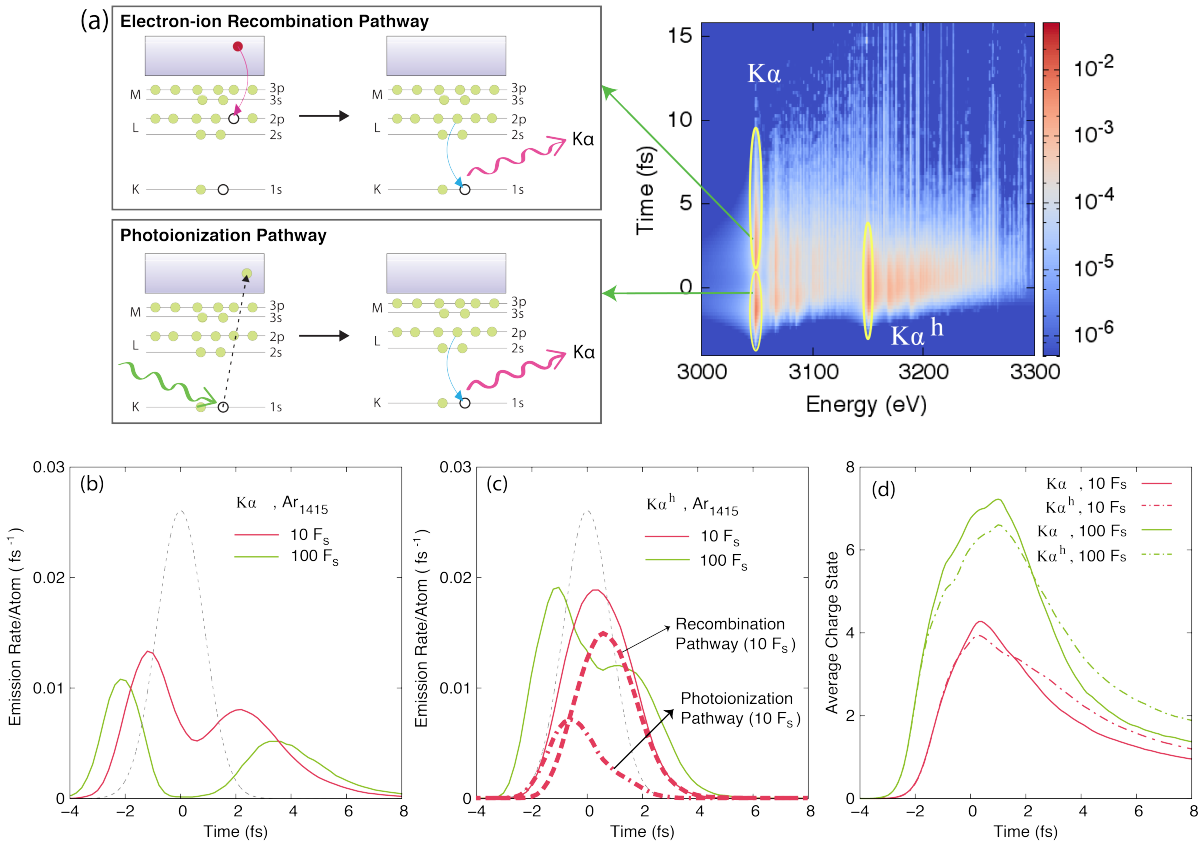

FIG. 4. (Color online) (a) Two fluorescence pathways of $K\alpha$ from electron-ion recombination and photoionization. Fluence dependence of the photoionization and recombination pathways (b) $K\alpha$ and (c) $K\alpha^h$ emission. (d) Average charge state of atoms emitting $K\alpha$ and $K\alpha^h$ via the recombination pathways. In panel (b), (c) and (d), the red lines (dark solid and dot-dashed line in grayscale) and green lines (light solid and dot-dashed line in grayscale) are profiles obtained for 10 and 100 F_s respectively.

shifted to a later time, and they are now well-separated from the photoionization pathway events, as shown in Fig. 4 (b). This because atoms are ionized to a higher charged state and they require more electron-ion recombination events to return to the $K\alpha$ fluorescence state.

For $K\alpha^h$, the emission profile is a single-peak distribution at 10 F_s. Our back-analysis shows, like the $K\alpha$ processes, both recombination pathways and photoionization pathways contribute to the $K\alpha^h$ yield. But, unlike the $K\alpha$ processes, the timing of these two pathways

are closely overlapped. Figure 4 (c) shows that the broad distributions of the photoionization and recombination pathways peak at t = -0.5 fs and 0.2 fs respectively. We note that, in comparison to $K\alpha$, the photoionization pathways of $K\alpha^h$ tend to take place later than those of $K\alpha$. This is because the direct photoionization pathways of $K\alpha^h$ require two photon absorption events, whereas those of $K\alpha$ require one photon absorption. As for the recombination pathways, Fig. 4(d) shows that the average charge state of the atoms that undergo $K\alpha^h$ via the recombination pathways reaches a maximum of about 4+, slightly lower than that of $K\alpha$, indicating that 2 recombination events are needed to reach the DCHS. As a result, the recombination pathways of $K\alpha^h$ take place earlier than those of $K\alpha$. At 100 F_s, Fig. 4 (c) shows that a double-peaked structure emerges for $K\alpha^h$. In particular, the emission from the photoionization pathways peak near t = -1 fs, which is earlier than those at 10 F_s. Also, the emission via the recombination pathways is pushed to a later time as the 100-F_s pulse produces a higher charge state (see Fig. 4 (d)) and it takes more recombination events (i.e. more time) to return to the fluorescence state (DCHS) for $K\alpha^h$.

B. Size Dependence

To understand the fluorescence dynamics in extended systems as a function of size, we compared the fluorescence processes in 10 systems, including Ar atom and 9 icosahedral clusters. These clusters are Ar_{13}, Ar_{147}, Ar_{561}, Ar_{1415}, Ar_{3871}, Ar_{12431}, Ar_{28741}, Ar_{55309} and, Ar_{149171}, and they have 1, 3, 5, 7, 10, 15, 25 and 35 icosahedral shells enclosing a center atom respectively. In these clusters, the shortest distance between a pair of Ar atoms is 3.76 Å. These systems are exposed to a 5-keV, 2-fs pulse with a fluence of 10 F_s.

Fig. 5 shows that the average per atom fluorescence yield of $K\alpha$ and $K\alpha^h$ emission from small systems ($\leq Ar_{147}$) decreases with size. The reduction of fluorescence yield is due to the probability of electron-impact ionization increases with system size, and this process depletes the population of the fluorescence states. The impact of this size dependence is revealed in Fig. 6, in which the larger clusters are ionized to a higher charge state during the rise of the x-ray pulse. Similar to electron-impact ionization, the probability of electron-ion recombination also increases with system size. For example, the recombination events lead to a small charge state reduction in Ar_{147} after the peak of the XFEL pulse, as shown in Fig. 6. However, in these systems, the number of $K\alpha$ and $K\alpha^h$ emission events via recombination

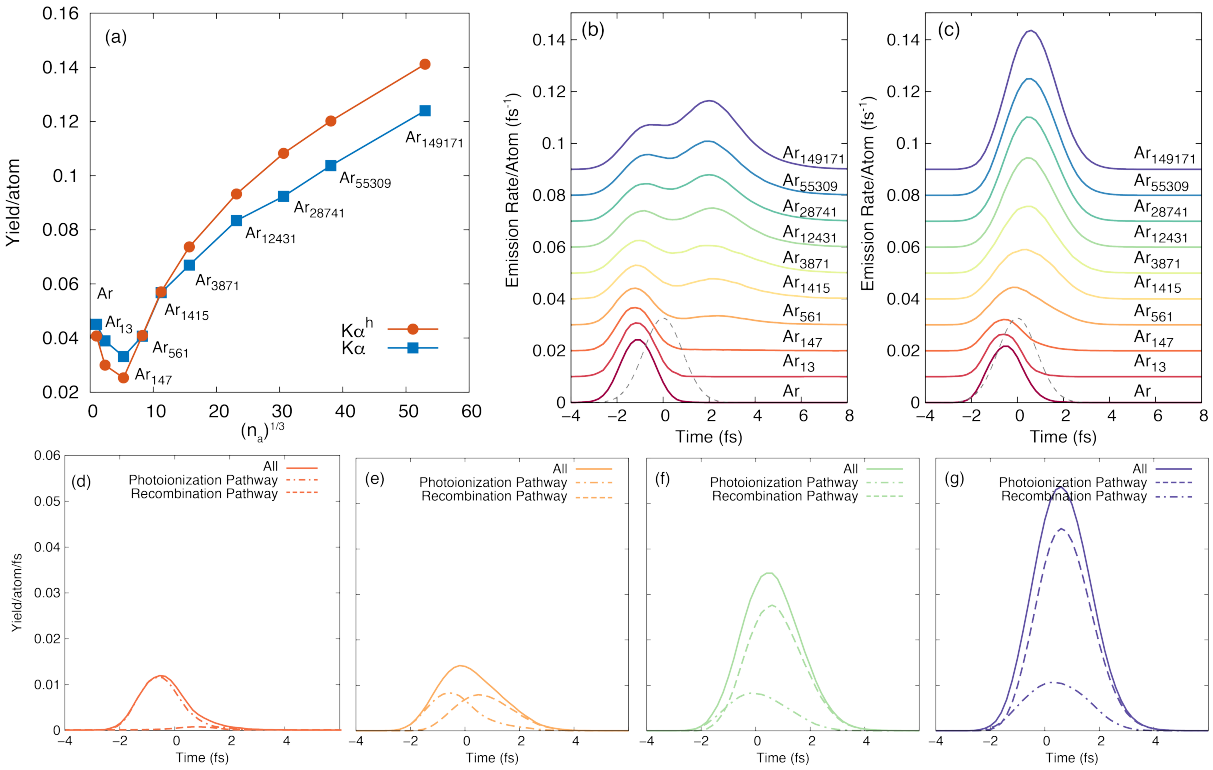

FIG. 5. (Color online) (a) Fluorescence yield as a function of the cube root of the number of atoms (n_a) for an incident intensity of 10 F_s. Temporal emission profile of (b) $K\alpha$ and (c) $K\alpha^h$ for Ar clusters with different number of atoms. Each system is exposed to a 5-keV, 2-fs and 10-F_s pulse. The dashed line in panel (b) and (c) shows the temporal x-ray profile. The temporal emission profiles of $K\alpha^h$ via the photoionization pathway (dashed-dot line) and the recombination pathway (dash line) are extracted for (d) Ar_{147}, (e) Ar_{561}, (f) Ar_{12431}, and (g) Ar_{149171}.

pathways are small and the fluorescence events are mainly through the direct photoionization pathway (for example, see Fig. 5 (d) for $K\alpha^h$ emission events in Ar_{147}). The reason is that the recombination pathways require many recombination events and longer times to reach $K\alpha$ and $K\alpha^h$ fluorescence states from the highly charged ions produced earlier in the pulse, and this requirement is unlikely less to be achieved since ionized electrons escape small clusters rapidly and the structures disintegrate during the pulse.

For systems larger than Ar_{147}, the average per atom yield of $K\alpha$ and $K\alpha^h$ emission increases with system size, as found in Fig. 5. In these systems, both recombination and direct photoionization pathways contribute to $K\alpha$ and $K\alpha^h$ production. We find that the

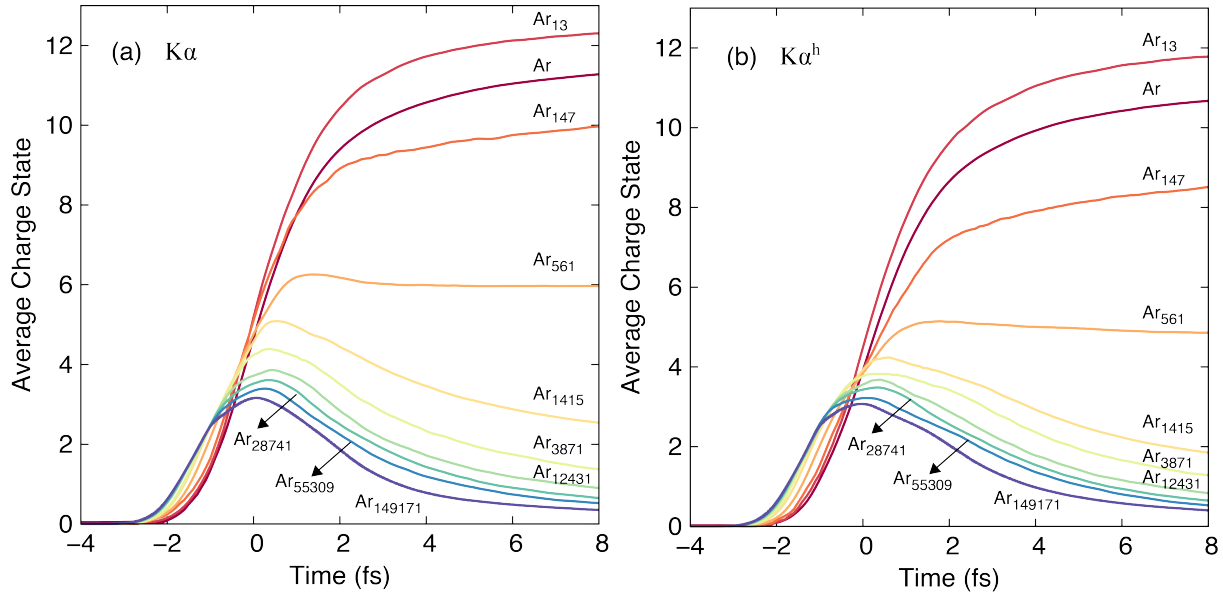

FIG. 6. (Color online) Average charge state of the atoms undergo (a) $K\alpha$ and (b) $K\alpha^h$ as a time function of time for various cluster sizes.

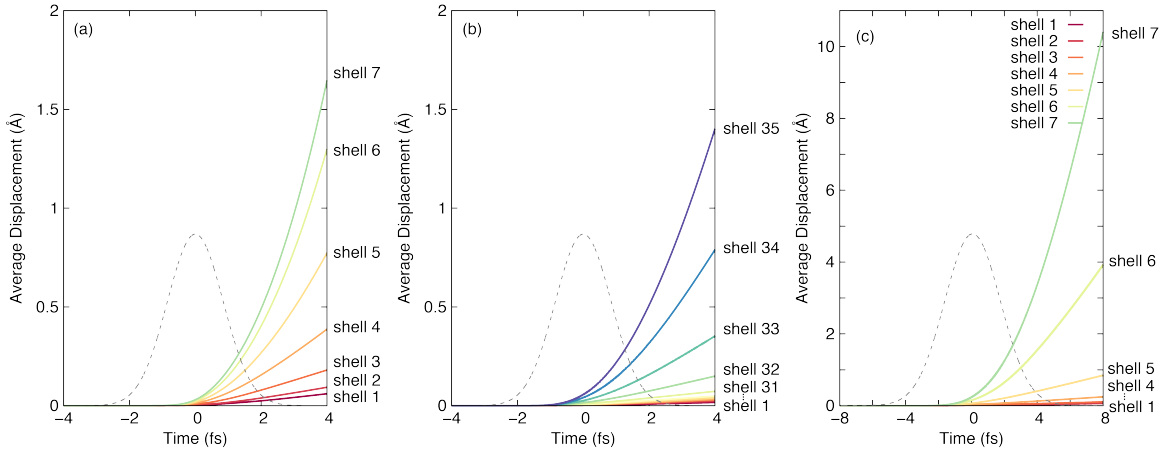

FIG. 7. (Color online) Average displacement of atoms in different shell in a (a) Ar_{1415} (b) Ar_{149171} in a 2-fs, 10-F_s pulse. There are 7 and 35 shells in Ar_{1415} and Ar_{149171}, respectively. Panel (c) is for Ar_{1415} in a 4-fs pulse.

enhancement in emission correlates with the recombination pathways becoming more dominant as the system size increases. Here, a larger system enables a stronger electron-trapping Coulomb potential inside the cluster volume, facilitating the creation of a dense electron environment that enhances the probability of electron-ion recombination [29, 55] and leading

to a smaller average charge state, as shown in Fig. 6. The impact of the increasing dominance of the recombination pathways is evident in the temporal emission profile of $K\alpha$ and $K\alpha^h$. In the case of $K\alpha$ emission, Fig. 5 (b) shows that the height of the peak associated with recombination pathways increases with system size. We note that the position of this peak shifts slightly from t = 2.2 fs in Ar_{1415} to t = 2.0 fs in Ar_{149171}. This is because, in comparison to Ar_{1415}, Ar_{149171} has a higher probability of electron-ion recombination and enables a dense electron environment to establish earlier for the fluorescence events via the recombination pathways.

For the $K\alpha^h$, the temporal emission profiles in these large systems ($> Ar_{147}$) remain a single-peak distribution since the timings of the photoionization and recombination pathway have significant temporal overlap. Figure 5 shows that the temporal emission profiles of these two $K\alpha^h$ pathways and their relative weights depend on the cluster size. Again, the recombination pathways become increasingly important as the cluster size increases. As a result, the temporal emission profile of Ar_{149171} peaks at a later time than that of Ar_{561}. Also, our result shows that the width of the temporal emission profile of Ar_{149171} is smaller than that of Ar_{561}. This is because in Ar_{149171} the temporal emission profile for the photoionization pathways peaks at a later time and overlaps more with the profile for the recombination pathways. This change in the temporal emission profile for the photoionization pathways results from a high probability of recombination in Ar_{149171} which produces an increased population of neutral atoms within the pulse duration, such that some of these atoms undergo $K\alpha^h$ via the photoionization pathways.

For imaging applications, one needs to connect the temporal fluorescence profile with the time-dependent XFEL-induced motion of the emitters. For fluorescence imaging, it is also important to find imaging conditions that minimize structure distortion. For our 2-fs, 5-keV, 10-F_s pulse, rapid ionization in the cluster volume leads to structural distortion of the cluster. Fig. 7 shows that the clusters expand rapidly after the peak of the pulse. The expansion rate of the cluster is spatially non-uniform and depends on the cluster size. For Ar_{1415}, its outer two layers of atoms expand more than a_0 at 2 fs after the peak of the pulse. The large cluster has a smaller expansion rate, the outermost layers also move close to a_0 at t = 2 fs. We found that 33% and 43% of the $K\alpha$ events in Ar_{1415} and Ar_{149171} take place at t $\geq$ 2 fs, i.e. when the cluster structures have been distorted by a_0. In contrast, only 11% and 12% of the $K\alpha^h$ events in Ar_{1415} and Ar_{149171} occur after t = 2 fs. Thus, the narrow

temporal emission profile combined with the higher yield suggests that the $K\alpha^h$ emission line can be a good candidate for fluorescence imaging of nanosized systems in an intense XFEL pulse.

We note that the induced structure distortion will add noise to the fluorescence imaging approach. But, based on the result of our previous work of the scattering of Ar clusters in intense XFEL pulse [16], we anticipate that the 1-a_0 expansion of outer layers in a 2-fs, 10-F_s pulse will not significantly hinder reconstruction of the whole geometry via the fluorescence approach. In that work, we showed that reconstruction of the atomistic structure of Ar clusters from the scattering pattern obtained in the face of damage is possible, even when the atoms move more than 1 a_0 during a 2-fs pulse and substantial noise from delocalized electrons is present. For a 4-fs pulse, Fig. 7 (c) shows that the outer two layers will expand more than 3 a_0 and 6 a_0 by the end of the pulse (t = 4 fs) while the atoms in the inner layers are displaced by a_0 or less. This suggests that fluorescence imaging with this 4-fs pulse will still be feasible for imaging the structure of the inner layers.

IV. DISCUSSION AND SUMMARY

In summary, we have investigated the x-ray emission dynamics of clusters as a function of fluence and cluster size. Our fluence dependence study shows that the fluorescence profile of single atoms and clusters are similar in the weak field regime, where the fluorescence dynamics depends mainly on the lifetime of the fluorescence state and XFEL pulse duration. In this regime, $K\alpha$ would be a better choice for fluorescence imaging as its yield can be orders of magnitude higher than $K\alpha^h$. However, in an intense x-ray pulse, fluorescence dynamics can be strongly influenced by incident fluence and system size. In an atom, an intense x-ray pulse can shorten the emission time as sequential multi-photon absorption interrupts and competes with inner-shell decay. In comparison, the temporal profile of cluster x-ray emission in an intense x-ray pulse is very different from the atomic profile. Already in a cluster with hundreds of atoms, electron-ion recombination processes enable additional pathways for fluorescence transitions, giving rise to an enhanced $K\alpha$ and $K\alpha^h$ emission yield and extended emission time. The electron-ion recombination pathways are found to be increasingly important in large systems. Our calculation suggests $K\alpha^h$ can be advantageous relative to $K\alpha$ since the $K\alpha^h$ has a more compact emission time, such that the emission

takes place before the onset of XFEL-induced structural damage.

In the future, we plan to investigate the feasibility/potential of achieving both atomic and elemental resolution of in heterogeneous systems with fluorescence imaging. Due to the elemental specificity of the fluorescence process, the obtained fluorescence intensity correlation will be sensitive to the incident photon energy. By comparing the correlation obtained below and above the absorption edge, one might be able to extract the distribution of a particular element within a complex system.

---

[1] C. Bostedt, S. Boutet, D. M. Fritz, Z. Huang, H. J. Lee, H. T. Lemke, A. Robert, W. F. Schlotter, J. J. Turner, and G. J. Williams, "Linac Coherent Light Source: The first five years," Rev. Mod. Phys. **88,** 015007 (2016).

[2] L. Young, K. Ueda, M. Gühr, P. H. Bucksbaum, M. Simon, S. Mukamel, N. Rohringer, K. C. Prince, C. Masciovecchio, M. Meyer, *et al.*, "Roadmap of ultrafast x-ray atomic and molecular physics," J. Phys. B **51,** 032003 (2018).

[3] R. Neutze, R. Wouts, D. van der Spoel, E. Weckert, and J. Hajdu, "Potential for biomolecular imaging with femtosecond X-ray pulses," Nature **406,** 752 (2000).

[4] H. N. Chapman, A. Barty, M. J. Bogan, S. Boutet, M. Frank, S. P. Hau-Riege, S. Marchesini, B. W. Woods, S. Bajt, W. H. Benner, *et al.*, "Femtosecond diffractive imaging with a soft-X-ray free-electron laser," Nature Phys. **2,** 839 (2006).

[5] M. M. Seibert, T. Ekeberg, F. R. N. C. Maia, M. Svenda, J. Andreasson, O. Jonsson, D. Odic, B. Iwan, A. Rocker, D. Westphal, *et al.*, "Single mimivirus particles intercepted and imaged with an X-ray laser," Nature **470,** 78 (2011).

[6] T. Ekeberg, M. Svenda, C. Abergel, F. R. Maia, V. Seltzer, J.-M. Claverie, M. Hantke, O. Jonsson, C. Nettelblad, G. van der Schot, *et al.*, "Three-Dimensional Reconstruction of the Giant Mimivirus Particle with an X-Ray Free-Electron Laser," Phys. Rev. Lett. **114,** 098102 (2015).

[7] N. D. Loh, C. Y. Hampton, A. V. Martin, D. Starodub, R. G. Sierra, A. Barty, A. Aquila, J. Schulz, L. Lomb, J. Steinbrener, *et al.*, "Fractal morphology, imaging and mass spectrometry of single aerosol particles in flight," Nature **486,** 513 (2012).

[8] J. N. Clark, L. Beitra, G. Xiong, A. Higginbotham, D. M. Fritz, H. T. Lemke, D. Zhu, M.

Chollet, G. J. Williams, M. Messerschmidt, *et al.*, "Ultrafast Three-Dimensional Imaging of Lattice Dynamics in Individual Gold Nanocrystals," Science **341,** 56 (2013).

[9] T. Gorkhover, S. Schorb, R. Coffee, M. Adolph, L. Foucar, D. Rupp, A. Aquila, J. D. Bozek, S. W. Epp, B. Erk, *et al.*, "Femtosecond and nanometre visualization of structural dynamics in superheated nanoparticles," Nat. Photon. **10,** 93 (2016).

[10] K. R. Ferguson, M. Bucher, T. Gorkhover, S. Boutet, H. Fukuzawa, J. E. Koglin, Y. Kumagai, A. Lutman, A. Marinelli, M. Messerschmidt, *et al.*, "Transient lattice contraction in the solid-to-plasma transition," Sci. Adv. **2,** e1500837 (2016).

[11] A. Aquila, A. Barty, C. Bostedt, S. Boutet, G. Carini, D. dePonte, P. Drell, S. Doniach, K. H. Downing, T. Earnest, *et al.*, "The linac coherent light source single particle imaging road map," Struct. Dyn. **2,** (2015).

[12] L. F. Gomez, K. R. Ferguson, J. P. Cryan, C. Bacellar, R. M. P. Tanyag, C. Jones, S. Schorb, D. Anielski, A. Belkacem, C. Bernando, *et al.*, "Shapes and vorticities of superfluid helium nanodroplets," Science **345,** 906 (2014).

[13] H. M. Quiney, and K. A. Nugent, "Biomolecular imaging and electronic damage using x-ray free-electron lasers," Nat. Phys. **7,** 142 (2011).

[14] U. Lorenz, N. M. Kabachnik, E. Weckert, and I. A. Vartanyants, "Impact of ultrafast electronic damage in single-particle x-ray imaging experiments," Phys. Rev. E **86,** 051911 (2012).

[15] B. Ziaja, H. N. Chapman, R. Fustlin, S. Hau-Riege, Z. Jurek, A. V. Martin, S. Toleikis, F. Wang, E. Weckert, and R. Santra, "Limitations of coherent diffractive imaging of single objects due to their damage by intense x-ray radiation," New Journal of Physics **14,** 115015 (2012).

[16] P. J. Ho, C. Knight, M. Tegze, G. Faigel, C. Bostedt, and L. Young, "Atomistic three-dimensional coherent x-ray imaging of nonbiological systems," Phys. Rev. A **94,** 063823 (2016).

[17] R. H. Brown, and R. Q. Twiss, "Correlation between Photons in two Coherent Beams of Light," Nature **177,** 27 EP (1956).

[18] R. J. Glauber, "The Quantum Theory of Optical Coherence," Phys. Rev. **130,** 2529 (1963).

[19] C. Thiel, J. von Zanthier, T. Bastin, E. Solano, and G. S. Agarwal, "Generation of Symmetric Dicke States of Remote Qubits with Linear Optics," Phys. Rev. Lett. **99,** 193602 (2007).

[20] T. Dertinger, R. Colyer, G. Iyer, S. Weiss, and J. Enderlein, "Fast, background-free, 3D super-resolution optical fluctuation imaging (SOFI)," Proceedings of the National Academy

of Sciences **106,** 22287 (2009).

[21] D. Gatto Monticone, K. Katamadze, P. Traina, E. Moreva, J. Forneris, I. Ruo-Berchera, P. Olivero, I. P. Degiovanni, G. Brida, and M. Genovese, "Beating the Abbe Diffraction Limit in Confocal Microscopy via Nonclassical Photon Statistics," Phys. Rev. Lett. **113,** 143602 (2014).

[22] H. Yu, R. Lu, S. Han, H. Xie, G. Du, T. Xiao, and D. Zhu, "Fourier-Transform Ghost Imaging with Hard X Rays," Phys. Rev. Lett. **117,** 113901 (2016).

[23] S. Oppel, R. Wiegner, G. S. Agarwal, and J. von Zanthier, "Directional Superradiant Emission from Statistically Independent Incoherent Nonclassical and Classical Sources," Phys. Rev. Lett. **113,** 263606 (2014).

[24] D. Pelliccia, A. Rack, M. Scheel, V. Cantelli, and D. M. Paganin, "Experimental X-Ray Ghost Imaging," Phys. Rev. Lett. **117,** 113902 (2016).

[25] A. Classen, F. Waldmann, S. Giebel, R. Schneider, D. Bhatti, T. Mehringer, and J. von Zanthier, "Superresolving Imaging of Arbitrary One-Dimensional Arrays of Thermal Light Sources Using Multiphoton Interference," Phys. Rev. Lett. **117,** 253601 (2016).

[26] R. Schneider, T. Mehringer, G. Mercurio, L. Wenthaus, A. Classen, G. Brenner, O. Gorobtsov, A. Benz, D. Bhatti, L. Bocklage, *et al.*, "Quantum imaging with incoherently scattered light from a free-electron laser," Nature Physics **14,** 126 (2017).

[27] A. Classen, K. Ayyer, H. N. Chapman, R. Röhlsberger, and J. von Zanthier, "Incoherent Diffractive Imaging via Intensity Correlations of Hard X Rays," Phys. Rev. Lett. **119,** 053401 (2017).

[28] J. Stöhr, "Overcoming the diffraction limit by multi-photon interference: a tutorial," Adv. Opt. Photon. **11,** 215 (2019).

[29] D. Rupp, L. Flückiger, M. Adolph, T. Gorkhover, M. Krikunova, J. P. Müller, M. Müller, T. Oelze, Y. Ovcharenko, B. Röben, *et al.*, "Recombination-Enhanced Surface Expansion of Clusters in Intense Soft X-Ray Laser Pulses," Phys. Rev. Lett. **117,** 153401 (2016).

[30] B. Schtte, T. Oelze, M. Krikunova, M. Arbeiter, T. Fennel, M. J. J. Vrakking, and A. Rouze, "Recombination dynamics of clusters in intense extreme-ultraviolet and near-infrared fields," New Journal of Physics **17,** 033043 (2015).

[31] M. Arbeiter, C. Peltz, and T. Fennel, "Electron-relocalization dynamics in xenon clusters in intense soft-x-ray fields," Phys. Rev. A **89,** 043428 (2014).

[32] M. Arbeiter, and T. Fennel, "Rare-gas clusters in intense VUV, XUV and soft x-ray pulses: signatures of the transition from nanoplasma-driven cluster expansion to Coulomb explosion in ion and electron spectra," New J. Phys. **13,** 053022 (2011).

[33] T. Gorkhover, M. Adolph, D. Rupp, S. Schorb, S. W. Epp, B. Erk, L. Foucar, R. Hartmann, N. Kimmel, K. U. Kuhnel, *et al.*, "Nanoplasma dynamics of single large xenon clusters irradiated with superintense X-ray pulses from the Linac coherent light source free-electron laser," Phys. Rev. Lett. **108,** 245005 (2012).

[34] L. Young, E. P. Kanter, B. Krässig, Y. Li, A. M. March, S. T. Pratt, R. Santra, S. H. Southworth, N. Rohringer, L. F. DiMauro, *et al.*, "Femtosecond electronic response of atoms to ultra-intense X-rays," Nature **466,** 56 (2010).

[35] G. Doumy, C. Roedig, S.-K. Son, C. I. Blaga, A. D. DiChiara, R. Santra, N. Berrah, C. Bostedt, J. D. Bozek, P. H. Bucksbaum, *et al.*, "Nonlinear atomic response to intense ultrashort X rays," Phys. Rev. Lett. **106,** 083002 (2011).

[36] B. Rudek, S.-K. Son, L. Foucar, S. W. Epp, B. Erk, R. Hartmann, M. Adolph, R. Andritschke, A. Aquila, N. Berrah, *et al.*, "Ultra-efficient ionization of heavy atoms by intense X-ray free-electron laser pulses," Nat. Photon. **6,** 858 (2012).

[37] M. Hoener, L. Fang, O. Kornilov, O. Gessner, S. T. Pratt, M. Guhr, E. P. Kanter, C. Blaga, C. Bostedt, J. D. Bozek, *et al.*, "Ultraintense X-ray induced ionization, dissociation, and frustrated absorption in molecular nitrogen," Phys. Rev. Lett. **104,** 253002 (2010).

[38] E. P. Kanter, B. Krässig, Y. Li, A. M. March, P. Ho, N. Rohringer, R. Santra, S. H. Southworth, L. F. DiMauro, G. Doumy, *et al.*, "Unveiling and driving hidden resonances with high-fluence, high-intensity x-ray pulses," Phys. Rev. Lett. **107,** 233001 (2011).

[39] B. Rudek, D. Rolles, S.-K. Son, L. Foucar, B. Erk, S. Epp, R. Boll, D. Anielski, C. Bostedt, S. Schorb, *et al.*, "Resonance-enhanced multiple ionization of krypton at an x-ray free-electron laser," Phys. Rev. A **87,** 023413 (2013).

[40] P. J. Ho, C. Bostedt, S. Schorb, and L. Young, "Theoretical tracking of resonance-enhanced multiple ionization pathways in x-ray free-electron laser pulses," Phys. Rev. Lett. **113,** 253001 (2014).

[41] L. Schroedter, M. Müller, A. Kickermann, A. Przystawik, S. Toleikis, M. Adolph, L. Flückiger, T. Gorkhover, L. Nösel, M. Krikunova, *et al.*, "Hidden Charge States in Soft-X-Ray Laser-Produced Nanoplasmas Revealed by Fluorescence Spectroscopy," Phys. Rev. Lett. **112,**

183401 (2014).

[42] H. Iwayama, M. Nagasono, J. R. Harries, and E. Shigemasa, "Demonstration of up-conversion fluorescence from Ar clusters in intense free-electron-laser fields," Opt. Express **20,** 23174 (2012).

[43] H. Iwayama, J. R. Harries, and E. Shigemasa, "Transient charge dynamics in argon-cluster nanoplasmas created by intense extreme-ultraviolet free-electron-laser irradiation," Phys. Rev. A **91,** 021402 (2015).

[44] M. O. Krause, and J. H. Oliver, "Natural widths of atomic K and L levels, K Xray lines and several KLL Auger lines," Journal of Physical and Chemical Reference Data **8,** 329 (1979).

[45] P. J. Ho, and C. Knight, "Large-scale atomistic calculations of clusters in intense x-ray pulses," J. Phys. B: At. Mol. Opt. Phys. **50,** 104003 (2017).

[46] M. H. Chen, B. Crasemann, and H. Mark, "Relativistic K-shell Auger rates, level widths, and fluorescence yields," Phys. Rev. A **21,** 436 (1980).

[47] M. H. Chen, B. Crasemann, and H. Mark, "Effect of the Breit interaction on K x-ray hypersatellite spectra," Phys. Rev. A **25,** 391 (1982).

[48] B. Ziaja, Z. Jurek, N. Medvedev, V. Saxena, S.-K. Son, and R. Santra, "Towards Realistic Simulations of Macromolecules Irradiated under the Conditions of Coherent Diffraction Imaging with an X-ray Free-Electron Laser," Photonics **2,** 256 (2015).

[49] S. M. Vinko, O. Ciricosta, B. I. Cho, K. Engelhorn, H. K. Chung, C. R. Brown, T. Burian, J. Chalupsky, R. W. Falcone, C. Graves, *et al.*, "Creation and diagnosis of a solid-density plasma with an X-ray free-electron laser," Nature **482,** 59 (2012).

[50] S. M. Vinko, O. Ciricosta, and J. S. Wark, "Density functional theory calculations of continuum lowering in strongly coupled plasmas," Nat Commun **5,** 3533 (2014).

[51] O. Ciricosta, S. M. Vinko, H.-K. Chung, B.-I. Cho, C. R. Brown, T. Burian, J. Chalupsky, K. Engelhorn, R. W. Falcone, C. Graves, *et al.*, "Direct Measurements of the Ionization Potential Depression in a Dense Plasma," Phys. Rev. Lett. **109,** 065002 (2012).

[52] T. Tachibana, Z. Jurek, H. Fukuzawa, K. Motomura, K. Nagaya, S. Wada, P. Johnsson, M. Siano, S. Mondal, Y. Ito, *et al.*, "Nanoplasma Formation by High Intensity Hard X-rays," Sci. Rep. **5,** 10977 (2015).

[53] R. Abela, A. Alarcon, J. Alex, C. Arrell, V. Arsov, S. Bettoni, M. Bopp, C. Bostedt, H.-H. Braun, M. Calvi, *et al.*, "The SwissFEL soft X-ray free-electron laser beamline: Athos,"

Journal of Synchrotron Radiation 26 (2019).

[54] R. N. Coffee, J. P. Cryan, J. Duris, W. Helml, S. Li, and A. Marinelli, "Development of ultrafast capabilities for X-ray free-electron lasers at the linac coherent light source," Philosophical Transactions of the Royal Society A: Mathematical, Physical and Engineering Sciences **377,** 20180386 (2019).

[55] T. Fennel, K.-H. Meiwes-Broer, J. Tiggesbaumker, P.-G. Reinhard, P. M. Dinh, and E. Suraud, "Laser-driven nonlinear cluster dynamics," Rev. Mod. Phys. **82,** 1793 (2010).

[56] Z. Jurek, G. Faigel, and M. Tegze, "Dynamics in a cluster under the influence of intense femtosecond hard X-ray pulses," Eur. Phys. J. D **29,** 217 (2004).

V. ACKNOWLEDGEMENT

This material is based on work supported by the U.S. Department of Energy, Office of Basic Energy Sciences, Division of Chemical Sciences, Geosciences, and Biosciences through Argonne National Laboratory. Argonne is a U.S. Department of Energy laboratory managed by UChicago Argonne, LLC, under contract DE-AC02-06CH11357. This research used resources of the Argonne Leadership Computing Facility, which is a DOE Office of Science User Facility supported under Contract DE-AC02-06CH11357, through a 2018 ALCC award.

Appendix A: Initiation of Electron in MC/MD Calculation

At each time step, the total energy of the system, which includes the energy of all electrons and ions/atoms, are tracked. This energy remains constant unless photoabsorption or fluorescence takes place. In particular, the total energy increases in photoabsorption, whereas it decreases in fluorescence. When an ionization event occurs in an atom, its electronic configuration is updated in the MC step. Then, the number of active particles in the MD step increases from N to N+1, and an additional energy equal to the difference between the photon energy and orbital binding energy is added to the MD calculation. The position and velocity of the active electron is chosen to ensure this additional energy is accounted for and momentum conservation is satisfied. Our scheme is similar to that described in [56]. In particular, the electron is placed at a distance that is larger than the impact parameter of impact ionization, and we compute the potential energy of the system. Then, the kinetic

energy of the system can be determined. The direction of the velocity vector is chosen randomly, but it points away from the parent ion and it is subjected to the angular distribution of the differential cross section of the photoelectric effect. In the case that the potential energy of the system is larger than the total energy, we repeat the above step with a new position vector. In the case of multiple ionization events, we rescale the kinetic energy of individual particles with the same factor to ensure the total energy is accounted for. For Auger decay and electron impact ionization, the same procedure is used, except the angular distribution of the electron is assumed to be isotropic [56]. In three-body recombination, the number of bound electrons increases by 1 and the electronic configuration of the ion is modified in the MC step. In the MD step, the recombining electron is removed from the calculation, and the kinetic energy (velocity) of the ion and the nearby electron are adjusted such that the total energy and momentum remain constant.

For this work, we used a regularized Coulomb potential for the ion-ion and electron-electron interactions, $Z_1 Z_2/\sqrt{(r_{12}^2 + b^2)}$ where Z_1 and Z_2 are the charge of the particles and $b = 0.006$ Bohr is used for the soft-core potential. This softcore potential prevents the scenario of unstable dynamics when two electrons approach very close to one another. We point out the fluorescence spectrum obtained from an ensemble of calculations with a time step of 2 as is statistically identical to the result computed with a time step of 0.2 as.